



## **COMPARISON OF OPTICAL COHERENCE TOMOGRAPHY, X-RAY COMPUTED TOMOGRAPHY, AND CONFOCAL MICROSCOPY RESULTS FROM AN IMPACT DAMAGED EPOXY/E-GLASS COMPOSITE**

**Joy P. Dunkers**

**Daniel P. Sanders**

**Donald L. Hunston**

Polymer Composites Group, National Institute  
of Standards and Technology, Gaithersburg, Maryland, USA

**Matthew J. Everett**

Medical Technology Program, Lawrence Livermore  
National Laboratory, Livermore, California, USA

**William H. Green**

US Army Research Laboratory, Weapons and Materials  
Research Directorate, Aberdeen Proving Ground, Maryland, USA

*Optical coherence tomography (OCT) is an emerging technique for imaging of synthetic materials. OCT is attractive because it combines high sensitivity (> 90 dB), high resolution (5  $\mu\text{m}$  to 20  $\mu\text{m}$ ), and low cost, approximately US \$75 K. The value of any new technology is evaluated by how well it compares with existing methods. In this work, impact damage of an epoxy/E-glass composite is imaged using OCT, and the results were compared with micro-focus X-ray computed tomography. This technique is a good benchmark to compare with OCT because both*

Received 20 April 2001; in final form 18 October 2001.

This is one of a collection of articles honoring Hatsuo (Ken) Ishida, the recipient in February 2001 of *The Adhesion Society Award for Excellence in Adhesion Science*, Sponsored by 3M.

The authors gratefully acknowledge Dr. Mary McKnight of the Building Materials Division for the generous use of her confocal microscope and for helpful discussions. Thanks are due to Dr. Carl Schultheisz for his insight into composite failure. The research funding provided by Dr. Felix Wu of the NIST advanced Technology Program is also appreciated.

Present address of Matthew J. Everett: Optical Imaging, Zeiss Humphrey Systems, 5160 Hacienda Drive, Dublin, CA 94568, USA.

Address correspondence to J. P. Dunkers, Polymer Composites Group, 100 Bureau Drive, STOP 8541, NIST, Gaithersburg, MD 20899-8541, USA. E-mail: joy.dunkers@nist.gov

*techniques have the ability to locate features precisely and have comparable resolutions. OCT is considered to be a confocal technique so it was also compared to laser scanning confocal microscopy (LSCM). Contrast mechanisms, sensitivity, resolution, depth of penetration, and artifacts among the techniques are compared and contrasted. Also, impact damage features revealed using OCT are briefly discussed.*

**Keywords:** Optical coherence tomography; X-ray computed tomography; Confocal microscopy; Composites; Damage

## INTRODUCTION

Resistance to impact damage is extremely important for most composites. Such damage can initiate delamination, which can be a failure mode itself or the initial step in other failure processes. For example, impact damage tolerance is the basis for design in many aerospace applications since loss of compression strength *via* delamination is a critical design issue. When the impact energy is high enough, cracks are generated in the polymer matrix and at the fiber-matrix interface. The number, size, shape, and location of the cracks are important since those which lead to delamination are usually more harmful than those that do not. Because this is such an important failure mode, many studies have tried to develop matrix resins and composite designs that are more resistant to impact (often called damage-tolerant systems). Such studies have been hampered by the difficulty in quantifying impact damage non-destructively.

Ultrasound, acoustic emission, infrared thermography, and X-ray radiography have been traditionally used for the non-destructive evaluation (NDE) of many types of composite damage [1–7]. Other less frequently used composite NDE techniques have also been developed and are discussed elsewhere [8]. Ultrasound imaging is primarily used to observe defects with a resolution of hundreds of microns, works best with planar samples, and utilizes either through-transmission or back-scattering modes [3]. Ultrasonic measurements may be complicated by the requirement of a coupling medium between the transducer and composite [3], unless laser based ultrasonics are performed. Ultrasound suffers from a degradation of feature contrast by shadowing of strongly scattering features located from above the area of interest. In addition, ultrasound can successfully image voids and damage in carbon-fiber-reinforced composites. Acoustic emission (AE) monitors the stress waves generated by the abrupt internal stress redistribution in the composite caused by changes in the internal

structure. The AE technique records parameters such as AE event counts, peak energy levels, and total energies. Researchers attempt to correlate these parameters with certain types of damage [9, 10]. In infrared (IR) thermography, a composite is irradiated with heat, which produces thermal patterns. Defects alter the heat flow and, therefore, the thermal patterns in composites with defects are considerably different than those produced in the undamaged portion of the composite. This generates the contrast needed for flaw detection [5, 11]; however, the sensitivity of IR thermography has generally been limited to flaws near the surface. IR thermography and ultrasonics have been traditionally used for inspection of composite parts in an industrial setting because of their speed, low cost, and ease of use. Unfortunately, they are limited in their sensitivity and their ability to quantify the location of a defect.

X-ray based techniques are used extensively to evaluate damage and have been applied less frequently to the examination of voids and tow position. Most X-ray techniques rely on the contrast generated by variations in the attenuation of the X-ray beam to differentiate heterogeneity from undisturbed material and are non-contact. The best resolution requires the use of a dye tracer to increase contrast between the damage zones and the rest of the composite. Also, superposition of features can confound interpretation with conventional film radiography. All of these techniques suffer from the inability to locate the damage at a precise depth. Optical coherence tomography (OCT) can address this issue for glass-reinforced systems.

OCT is a confocal technique that is enhanced by interferometric rejection of out-of-plane photon scattering. As early as 1973, Sawatari [12] recognized the potential gains in sensitivity that result from combining coherent illumination and heterodyne detection in a precursor to OCT: the optical heterodyne scanning microscope. OCT was developed in the early 1990s and has been used extensively to image the human retina [13], skin and blood vessels [14], and the operating circulatory system of small live animals [15] with excellent clarity. Briefly, OCT uses a low coherence source such as a superluminescent fiber-optic diode laser with a fiber optic based Michelson interferometer. In this configuration, the composite is the fixed arm of the interferometer and the fiber optic acts as the confocal aperture. Reflections from heterogeneities within the sample are mapped as a function of thickness (z-axis) by path matching with the moving reference arm for any one position. Volume information is generated by translating the sample on a motorized stage through x- and y-axes. Quantitative information about the location and size of a feature within the composite is obtained. Practically, OCT can image

composites having a thickness of  $< 1$  cm with a spatial resolution from  $5\ \mu\text{m}$  to  $20\ \mu\text{m}$  with high sensitivity. Recently, resolutions of  $3\ \mu\text{m}$  have been reached with state-of-the art lasers, electronics, and optics [16]. Additionally, OCT systems have been built that are sensitive to birefringence [17]. In other words, the data drop-out from a change in polarization state in the sample arm relative to the reference arm can be eliminated by detecting the parallel and perpendicular polarizations, or the birefringence can be enhanced by displaying one polarization state.

One way to evaluate the success of any new technique is to compare it with existing measurement methods. In this work, OCT images on a particular region of damage will be cross-compared to laser scanning confocal microscopy (LSCM) and X-ray computed tomography (CT) because both these techniques have precise depth discrimination and are comparable or superior in resolution.

A more advanced version of radiography, X-ray CT relies on the measurement of transmitted radiation measured at many angles to reconstruct an image of the composite [18]. X-ray CT can be used to detect various heterogeneities such as resin/fiber distribution, anisotropic fiber structure, voiding and porosity, as well as damage events. However, there are some drawbacks. X-ray CT is not amenable to flat composites or composites that have a large length-to-width ratio. The X-ray transmission is limited by the density, size and atomic number of material and X-ray source available. The damage must have a separation to be detected. Perhaps the biggest drawback is the spatial resolution, which is typically  $500\ \mu\text{m}$  with a commercial system. With specialized sources and detectors, the spatial resolution can approach a few microns with objects millimeters in maximum dimensions [18].

An analog to OCT, LSCM has been used extensively in the biomedical arena [19]. LSCM utilizes coherent light focused to a diffraction-limited spot and variable pinholes to reject the image out-of-plane scatter and increase contrast and resolution of the object in the image plane when compared with conventional microscopy. The size of the pinhole and the numerical aperture of the objective primarily determine the resolution in the thickness or axial direction. The smaller the holes, the higher the resolution but the lower the intensity throughput. Object features in the order of  $0.2\ \mu\text{m}$  can be resolved in the transverse direction and  $0.1\ \mu\text{m}$  in the axial direction. OCT is only performed in reflection mode while LSCM is amenable to either reflection or transmission, and LSCM does not exhibit birefringence artifacts.

The comparison of OCT to LSCM is performed not because LSCM is traditionally a composite NDE technique, but because LSCM and OCT

are both confocal optical techniques. X-ray CT was chosen for comparison because it can image sample microstructure and damage at a known position within the sample for large sampling volumes. Images of the damage region will be presented from all three techniques. The images will be discussed in terms of resolution, sensitivity, depth of penetration and artifacts.

## EXPERIMENTAL

Details concerning the composite fabrication are provided in previous work [20]. The composite consists of unidirectional E-glass tows and epoxy resin. Each tow is approximately  $2\text{ mm} \times (0.5\text{ to }0.8\text{ mm})$  in dimension. The E-glass fibers were unsized. To generate the damage, the composite was secured in a vice and impacted with a blunt object at various places with various loads.

The OCT imaging system used in this study is schematically shown in Figure 1. A commercial superluminescent diode light source is used for the studies reported here. The source operates at  $1.3\ \mu\text{m}$  with an output power of up to 13 mW and a spectral bandwidth of 70 nm. The laser light is coupled into a single-mode fiber-optic Michelson

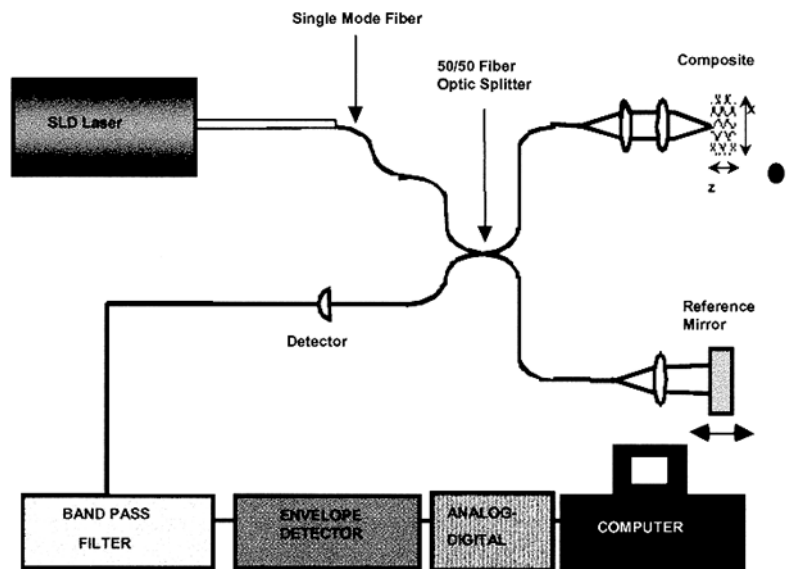


**FIGURE 1** Schematic representation of the solid state laser and OCT system layout.

interferometer and is delivered to both the reference mirror and the sample. The reference mirror is mounted on a rotating galvanometer, which is driven with a sawtooth voltage waveform. The interferometric signal is electronically filtered with a bandpass centered on the fringe or heterodyne frequency. The filtered fringe waveform is then demodulated, digitized and stored on a computer. Transverse and longitudinal scanning is performed using a computer-controlled motorized stage to translate the sample.

The sensitivity of the OCT system was measured to be 108 dB. Volumetric OCT images were taken at a low and a high resolution. The resolution along the axial, or z-axis, was  $15\ \mu\text{m}$  for both the high and low resolutions. For the low resolution images (LR-OCT), the sample was imaged using the  $5\times$  objective. All of the transverse resolutions are calculated assuming a Gaussian beam from confocal parameter measurements. Axes references are shown in Figure 2. The sampling volume was 6.0 mm along the x-axis, 6.0 mm along the y-axis, and 4.5 mm along the z-axis. The pixel size along the x-axis was  $20\ \mu\text{m}$ , along the y-axis was  $40\ \mu\text{m}$ , and along the z-axis was  $5\ \mu\text{m}$ . For the

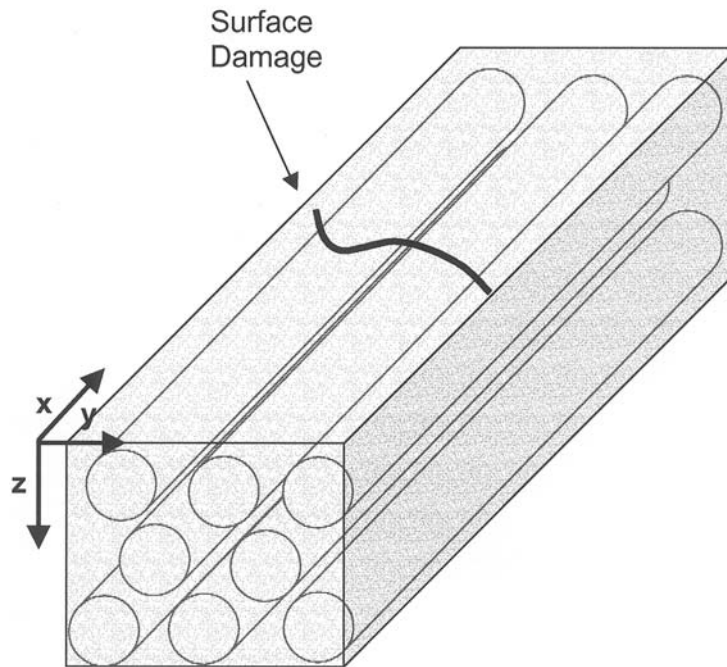


**FIGURE 2** Schematic of composite damage region of interest with axes.

high-resolution images (HR-OCT), the sample was imaged using the 26 $\times$  objective having a resolution of 6.9  $\mu\text{m}$  in the x-direction. The sampling volume was 3.0 mm along x, 3.0 mm along y, and 2.0 mm along z. The pixel size along the x-axis was 5  $\mu\text{m}$ , along the y axis was 5  $\mu\text{m}$ , and along the z axis was 5  $\mu\text{m}$ . All images are displayed as  $\log(\text{intensity})$ .

A volumetric set of x-z images was created by stepping the motorized stage along the y-axis. Each x-z slice was saved in IEEE floating point format. These slices were then input into a custom written MATLAB [21] program for image processing. Typical image processing operations included image cropping, rotation, and contrast enhancement. The images were then written out as hierarchical data format (HDF) files. The HDF files were read into the Noesys T3D volumetric rendering software for visualization.

A Zeiss laser scanning confocal microscope was used in reflection at 543 nm at 5 mW with a pinhole diameter of 99  $\mu\text{m}$ . The confocal images are a collage of 12 individual, 12-bit images collected with a 10 $\times$ /0.3 objective. The 12-bit individual images consisted of a 512  $\times$  512 area of pixels. The brightness of each image was manually adjusted to optimize image quality. The image collage represents an area of about 2 mm along the x-axis and 1.9 mm along the y-axis. The axial resolution is 15  $\mu\text{m}$ . This resolution was chosen in order for the LSCM images to be comparable with the OCT images.

For the X-ray CT, the sample was inspected using a customized ACTIS 600/420 computed tomography system designed and constructed by Bio-Imaging Research, Inc., and installed at the U.S. Army Research Laboratory (ARL) at Aberdeen Proving Ground (APG), Maryland. The system was designed to meet ARL performance specifications. It has a 420 keV X-ray tube with two focal spot sizes and a 160 keV microfocus X-ray tube with four focal spot sizes, the smallest being 10  $\mu\text{m}$ . It has a linear detector array (LDA) and an image intensifier (II) with a zoom lens and a charged-coupled device camera. Computed tomography scanning can be done using the LDA or the II detector. The system can scan in rotate-only (RO) and offset-RO mode using either source and the LDA or the II detector, and in translate-rotate (TR) mode using either source and the LDA detector. It can also perform digital radiography (DR) scans using the LDA or II detector. A dedicated embedded industrial computer system controls object scanning (*i.e.*, data collection) and image reconstruction, viewing, and processing. It uses an Intel Pentium 166 MHz central processing unit and customized components, including an accelerated display controller and multi-axis servo control, detector interface, and array processor boards.

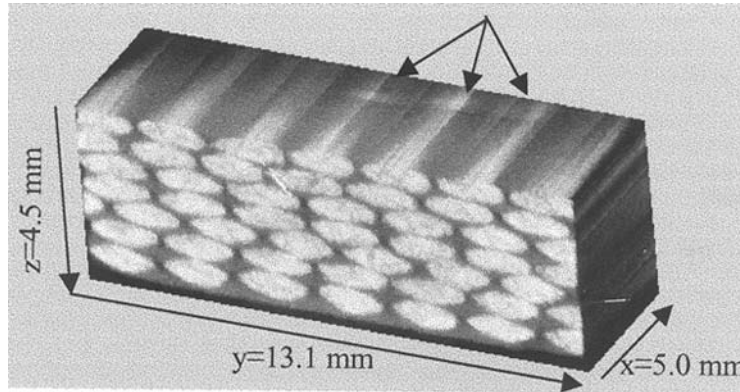
A five millimeter height section of the sample was scanned in RO mode using the 160 keV microfocus tube and the image intensifier. The sample was scanned over an area with visible indications of the flaw imaged by the OCT. The cross-sectional image plane is also the y-z plane shown in Figure 2. The source-to-object distance (SOD) and the source-to-image distance (SID) were 46.93 mm and 648.00 mm, respectively. The slice thickness and slice increment were 0.100 mm, resulting in contiguous scans. Scan time was about 1.5 min per slice with 51 slices required to scan the 5 mm section. Each slice was reconstructed to a 512 by 512 image matrix using 5120 views having a 13.40 mm field of view. Thus, the pixel size would be 26  $\mu\text{m}$  and the resolution is 52  $\mu\text{m}$ . The tube energy and current were 160 keV and 0.025 mA, respectively, and the focal spot was 10  $\mu\text{m}$ .

## RESULTS AND DISCUSSION

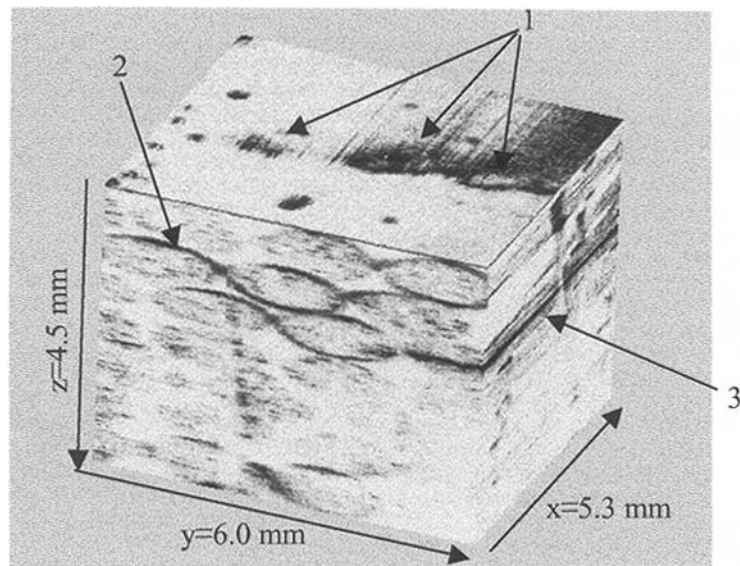
Before presenting the imaging results, it is necessary to clarify the position and orientation of features to be presented. A schematic of the composite and damage is shown in Figure 2. By convention, the plane along which each image is collected is the x-z plane for OCT. The glass tows that run parallel to the y-axis are composed of about 2000 individual E-glass fibers, each about (10 to 15)  $\mu\text{m}$  in diameter. Each tow is about 2 mm wide by (0.5 to 0.8)  $\mu\text{m}$  high. The data were collected by scanning perpendicular to the damage, and the damage runs parallel to the y-axis.

The impact experiment involved gripping the sample at one end (high x values in Figure 2) in a vice with the vice jaws against the top and bottom surfaces ( $z = 0$  and  $z = 4.5$ ). The other end of the sample (low x values) was free. The impact was directed at the center of the bottom surface in Figure 2, and the most visible surface damage occurred on the opposite or top surface. This damage runs roughly parallel to the y-axis so the x-z data scans are perpendicular to the damage.

A volumetric rendering of the X-ray CT results on the impact-damaged composite is shown in Figure 3a. Cross-sections of the tows are seen in the y-z plane. The tows run lengthwise along the x-axis. Unlike the OCT, the microstructure of the glass is clearly revealed throughout the entire thickness of the sample with some layers in a stacked configuration while others are more nested. Also, high contrast is maintained throughout the cross-section of a particular tow. The arrows in Figure 3a point to the surface damage shown faintly by the X-ray CT. This same damage is shown predominately in Figure 3b (arrow 1) by the OCT. As in Figure 3a, the tow cross-section can be



a.



b.

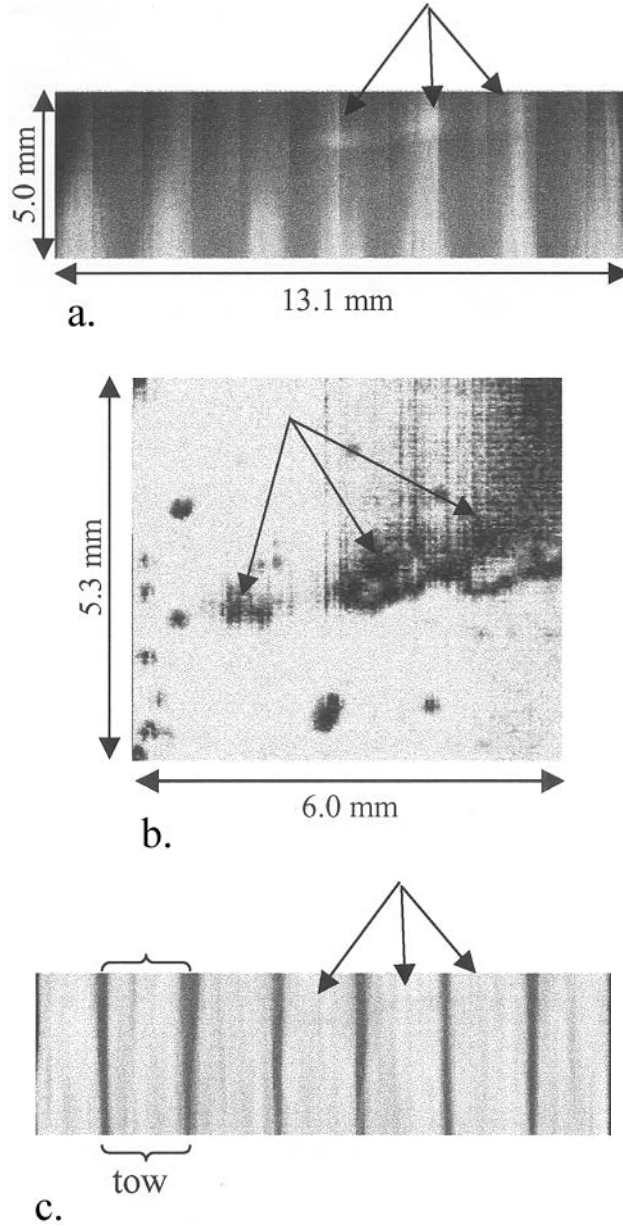
**FIGURE 3** Volumetric reconstruction of damage region of interest from a.) X-ray computed tomography and b.) optical coherence tomography.

seen in Figure 3b along the  $y$ - $z$  plane, and the tows run lengthwise in the  $x$ -direction. In Figure 3b, the contrast between the tows and epoxy is lower and more variable within a tow than in Figure 3a. The polyester stitching that holds a layer of fabric together is clearly seen

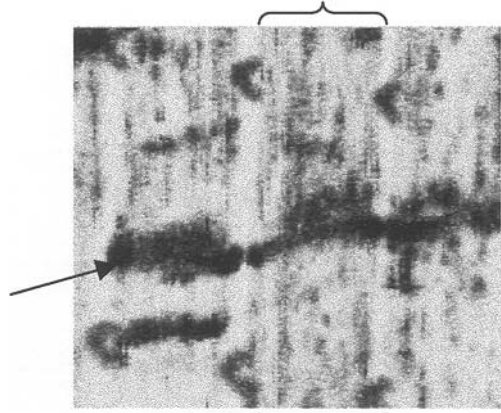
in the OCT results (arrow 2), but not in Figure 3a. The contrast generated by the difference in electron density between the carbon atoms in the stitching and the carbon atoms in the epoxy is not more than the approximately 0.2% required to differentiate between the two for X-ray CT. Arrow 3 in Figure 3b shows a crack running along the x direction. The highly reflecting nature of the crack shadows the features below it, making them almost invisible. Shadowing by highly reflecting features from above causes data drop-out artifacts in OCT images. This effect can be mitigated by collecting images from various faces of a sample. For a better comparison, both the OCT and X-ray CT were sliced at various x-y planes at a z distance from the surface.

Figure 4 is a comparison of the X-ray CT (a, c, e) and low resolution OCT images (B, D, F) at  $0\ \mu\text{m}$ ,  $340\ \mu\text{m}$ , and  $560\ \mu\text{m}$  from the top surface. The features represented in each slice are dependent upon resolution. Figures 4a and b show the top surface of the sample ( $0\ \mu\text{m}$ ). Arrows denote the surface damage in each image. The damage seen in Figure 4b involves kink band formation which is generally associated with failure due to compression loading along the fiber axis. This is a failure mode in which a band of shear deformation occurs in the matrix and across a group of fibers causing the fiber segments in the band to rotate so they are at an angle to the overall fiber direction. The fibers on either side of the band are displaced by the corresponding amount so they are still parallel but no longer aligned. The fibers generally break along the edges of the band and create a characteristic zigzag pattern [22]. The presence of kink bands can be rationalized by noting that the way the specimen is gripped and loaded means that the impact produces bending so the top half of the sample is subjected to compression. Further evidence for kink band formation will be presented later in this work. It is also interesting to note that more damage exists on the compression side of the specimen (top half) than on the tensile side (bottom half). This is unusual for a thermoset resin. Three factors may contribute to this. First, the resin is a low  $T_g$  material with a low cross-link density so it is tougher than the usual thermoset. Tougher resins are more likely to fail on the compression side as seen with thermoplastics. Second, the fiber-matrix interface in this system is believed to be weak since there was no effort to optimize the fiber surface treatment. This is supported by the evidence of debonding discussed later in this paper. Finally, when the sample is bent, the end of the grip used to hold the specimen may generate local stress concentrations on the compression side that help promote failure.

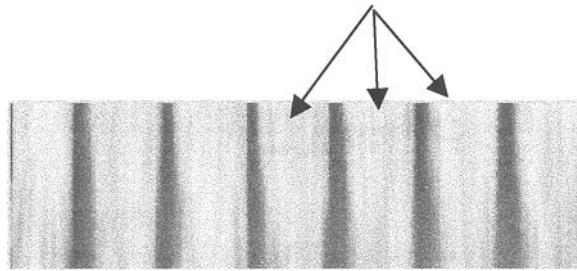
Figures 4c and d show the X-ray and OCT images  $340\ \mu\text{m}$  from the top surface. Excellent contrast between the fibers and matrix is maintained in Figure 4c. However, the crack is almost invisible. The



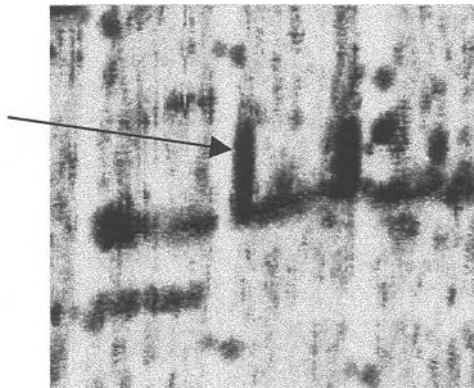
**FIGURE 4** x-y slices of the damage of interest at various distances along the z-axis: a.) X-ray CT, 0  $\mu\text{m}$ , b.) LR-OCT, 0  $\mu\text{m}$ , c.) X-ray CT, 340  $\mu\text{m}$ , d.) LR-OCT, 340  $\mu\text{m}$ , e.) X-ray, 550  $\mu\text{m}$ , and f.) LR-OCT, 550  $\mu\text{m}$ . Orientation is the same as Figure 2.



d. tow



e.



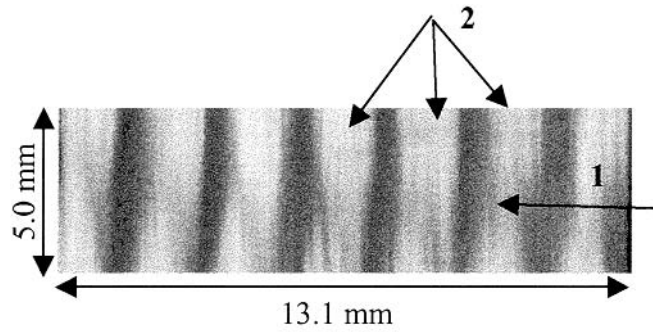
f.

**FIGURE 4** (*continued*).

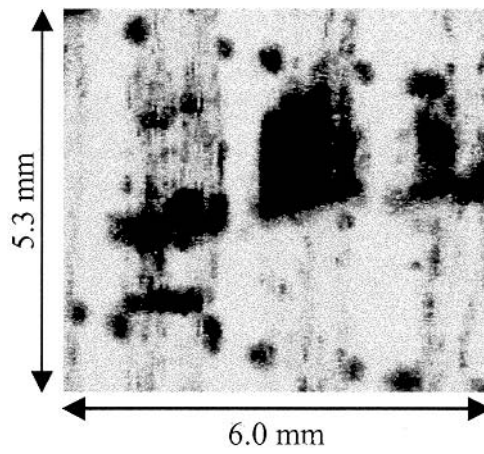
corresponding OCT image in Figure 4d reveals very different information. A crack generated by the impact damage that traverses all three tows is clearly visible as indicated by the arrow. Another small crack that travels across one tow is also seen as well as the “c” shaped objects in between the tows. The “c” shaped objects are polyester stitching. Dark, narrow regions in the fiber direction are also evident. These features can be assigned to channel voids induced during processing or to fiber/matrix de-bonding generated during impact. In the area surrounding the crack, these features appear at very high density and are, thus, assigned to fiber-matrix de-bonding. This will be shown more clearly in the high resolution OCT images. The initiation of an interesting damage pattern is shown in Figure 4f at  $550\ \mu\text{m}$  below the top surface. The damage travels transverse to the tows as in previous figures. However, two longitudinal cracks that move along the tow/epoxy interface are shown by the arrow. This type of damage is consistent with failure of a weak interface. No such features are observable in the X-ray results. It is well known that the X-ray absorption of different organic materials may not be sufficient to generate contrast. An X-ray based technique that may provide the sensitivity required to observe the damage and stitching clearly is phase-contrast X-ray CT (PC-XCT). In PC-XCT, the contrast is generated by the phase shift from different organic materials and is manifested in the fringes from the X-ray interferometer [22].

The damage discussed above further develops into a delamination zone beneath the first layer of tows at  $650\ \mu\text{m}$  from the top surface, shown in Figure 5b. In Figure 5a, the transition from the first to second layer of stacked tows is evidenced by the diffuse, gray regions that exist. An example of this is shown by arrow 1. Again, there is almost no evidence of the damage in Figures 5a (arrow 2), c and e. Figure 5d is the OCT image of the damage in the second layer of tows at  $850\ \mu\text{m}$  from the top surface. In Figure 5f, the damage is now  $1680\ \mu\text{m}$  from the top surface. The light region indicated by the arrow is a result of data drop-out from the crack above. The impact of the shadowing is better seen in Figure 6.

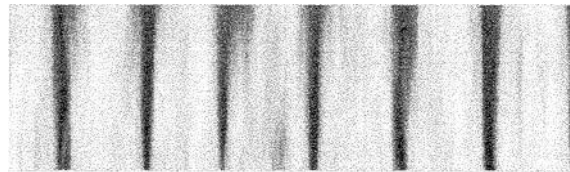
Figure 6 shows a comparison of the same region scanned through the top surface (Figure 6a) or through the bottom surface (Figure 6b). The scan is an x-z cross-section located 5.3 mm along the y-axis. In Figure 6a the kink band and related cracking are seen to propagate at an angle down through the composites. The shadowing created by this damage appears as a widening vertical streak indicated by arrow 2. This shadowing obscures any data in its path. One technique to cope with this is to collect data by scanning from a different direction. Figure 6b shows the approximately same location in the



a.

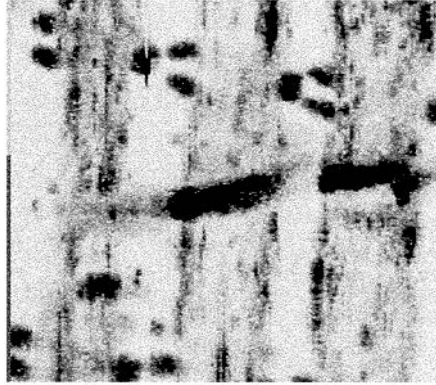


b.

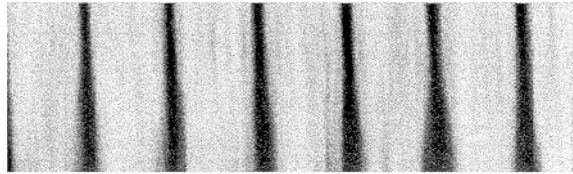


c.

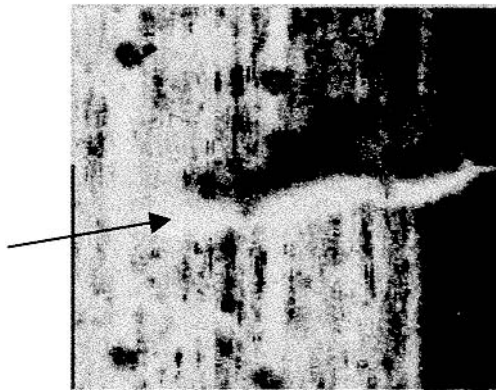
**FIGURE 5** x-y slices of the damage of interest at various distances from the top of the specimen along the z-axis: a.) X-ray CT, 650  $\mu\text{m}$ , b.) LR-OCT, 650  $\mu\text{m}$ , c.) X-ray CT, 850  $\mu\text{m}$ , d.) LR-OCT, 850  $\mu\text{m}$ , e.) X-ray, 1680  $\mu\text{m}$ , and f.) LR-OCT, 1680  $\mu\text{m}$ .



d.



e.



f.

**FIGURE 5** (continued).

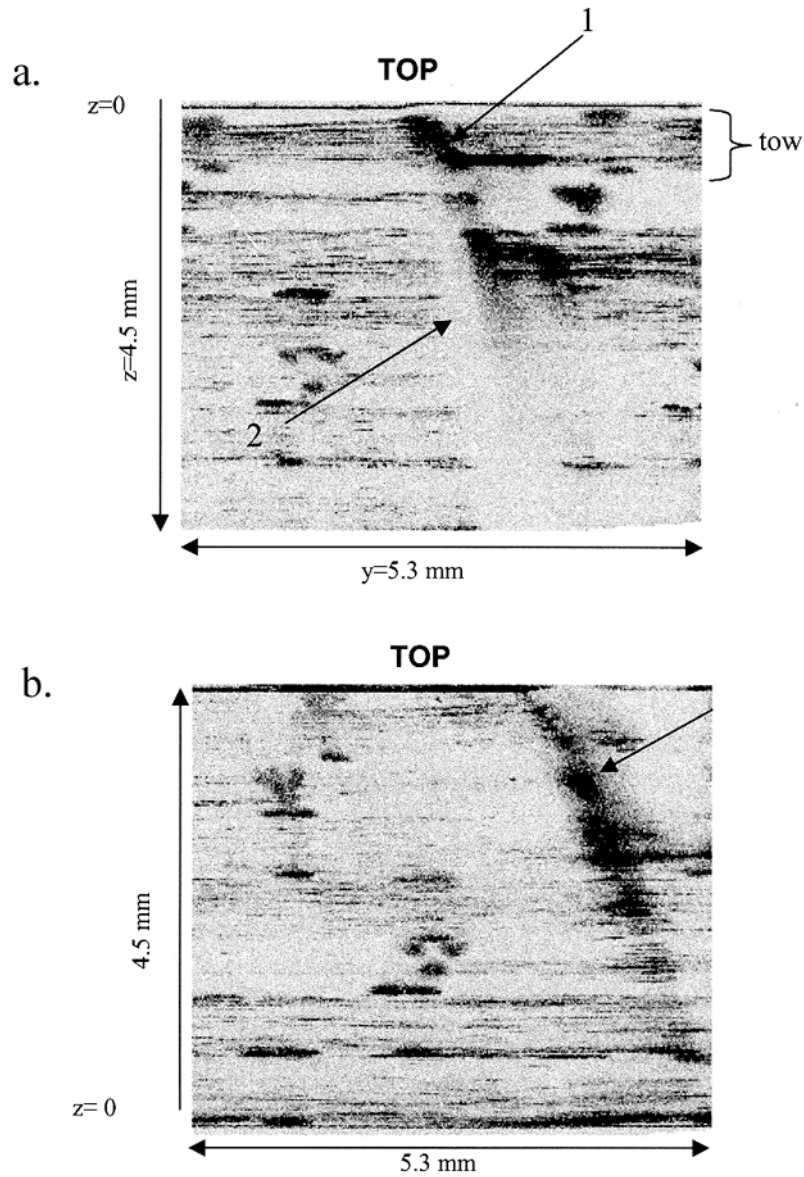


**FIGURE 6** LR-OCT x-z slices at a constant y position showing kink bands and longitudinal cracking: a.) Image collected with  $z=0$  plane facing up, b.) Image collected with  $z=4.5$  mm plane facing up.

composite but imaged from the bottom surface. The arrow reveals that the damage travels throughout almost the entire thickness of the composite.

Figures 7, 8, 9, and 12 compare the high resolution OCT images with the LSCM images along the x-y plane at various z depths from the top surface. Figure 7a is the LSCM image of the crack (arrow) at the surface of the composite. The shadows obscuring most of the damage results from the out-of-focus areas on the surface that were displaced during impact. The straight vertical and horizontal lines were scribed as a grid. Figure 7b shows the corresponding HR-OCT image at the surface of the sample. The white areas indicated by arrow 1 are regions of high reflectivity, meaning these regions are displaced upward when compared with the rest of the sample. Arrow 2 reveals a plane of fibers that been displaced upward during the impact. The crack runs along the right boundary of the white area (arrow 3). The black grid lines are also evident in this image.

Figure 8a is the LSCM collage of the sample 340  $\mu\text{m}$  below the top surface. In this image and in other LSCM images, only the damage is detected (arrow 1). LSCM does not have sufficient sensitivity to detect fiber architecture in addition to the damage. Diffuse damage in the matrix that bridges the two tows is shown by arrow 2. In contrast, the HR-OCT cross-section at 340  $\mu\text{m}$  from the top surface in Figure 8b shows the kink band region (arrow 1) and subsequent de-bond regions quite clearly (arrow 2). Additionally, OCT still has enough sensitivity to detect the glass fiber against the epoxy background. The LSCM results in Figure 9a have the same damage features as in the previous figures. The large delamination seen by the OCT in Figure 8 is again seen in Figure 9b (arrow) at 650  $\mu\text{m}$  from the surface. The fibers still retain good differentiation from the epoxy.

Evidence of kink banding is more clearly seen in Figure 10. In this figure, a section of the tow is pushed upward relative to the undisturbed tows as shown by arrow 1. The discontinuity resulting from the displacement of fibers is indicated by arrow 2. The fiber debonding is again seen by arrow 3.

The diffuse damage seen by the LSCM can also be viewed by the OCT if the image is reconstructed differently. Figure 11 shows the volumetric HR-OCT reconstruction of that damage region. In this view, many levels of gray are made transparent to access only the features of interest. Now the region of damage in between the tows shown so clearly by LSCM can be seen by the OCT as indicated by the arrow. Since each slice in the HR-OCT is 5  $\mu\text{m}$  in thickness, the combination of multiple slices may be required before a diffuse feature is revealed.

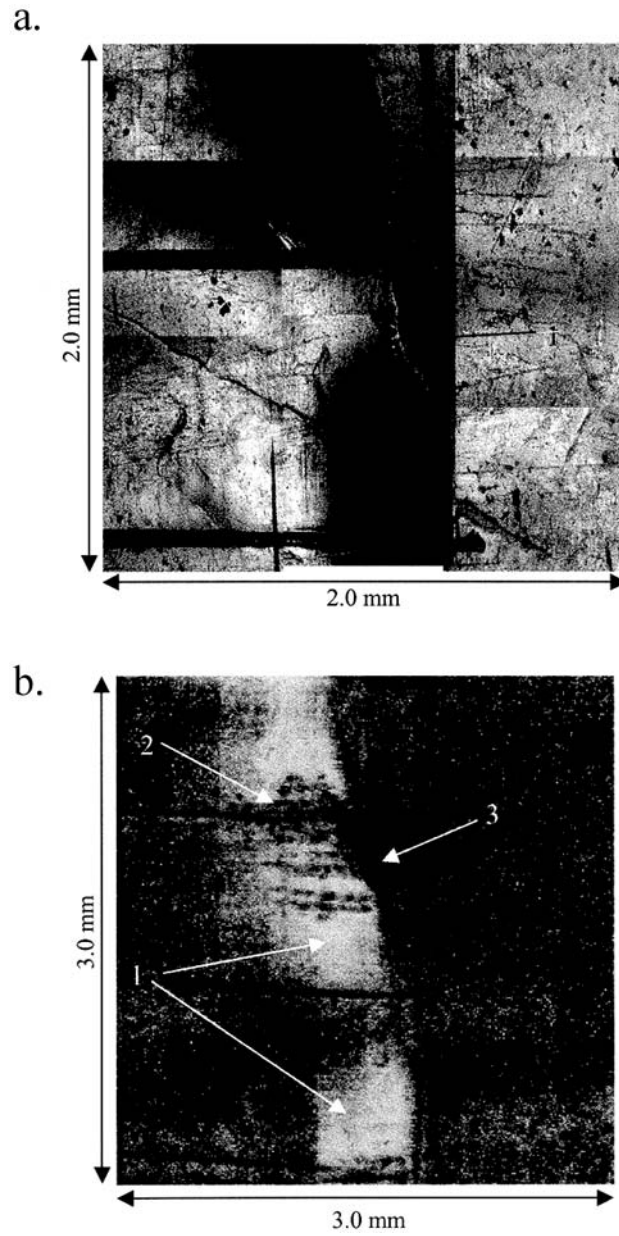


**FIGURE 7** Comparison of x-y images at  $0\ \mu\text{m}$  from the top surface: a.) LSCM and b.) HR-OCT.

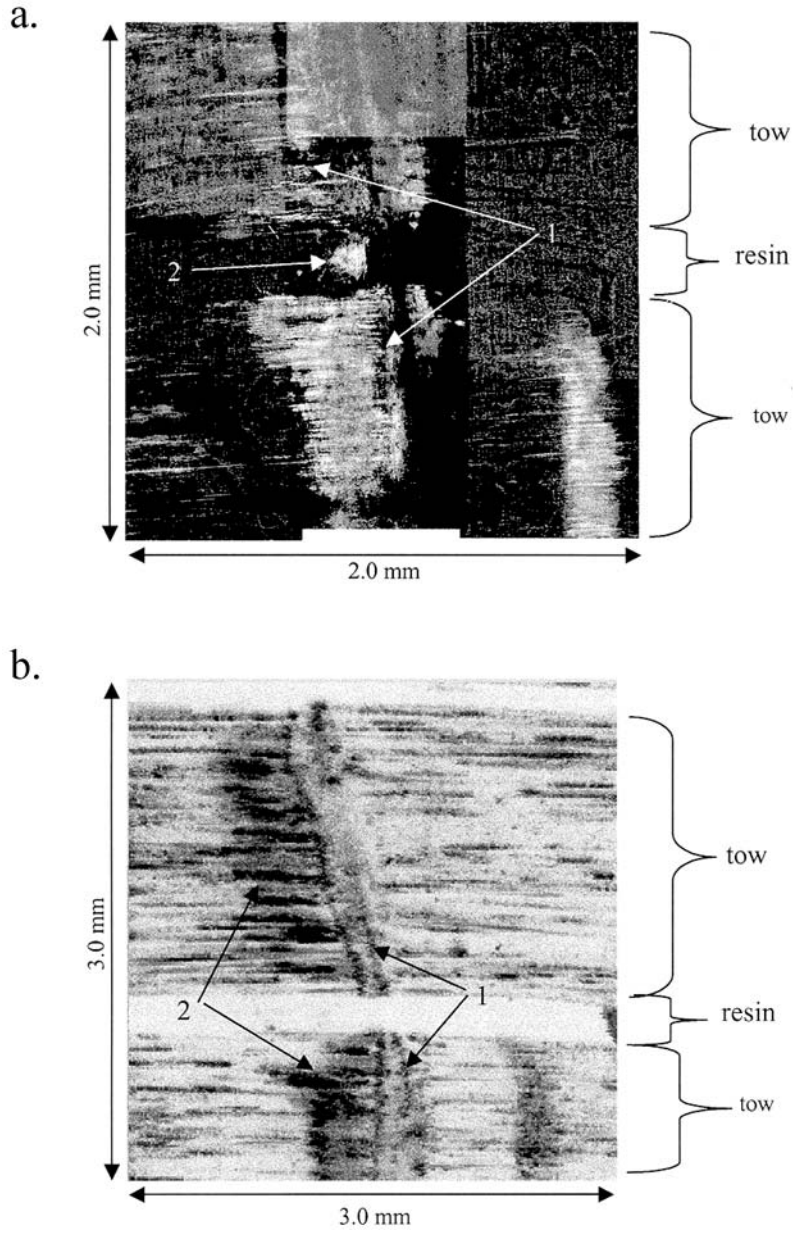


**FIGURE 8** Comparison of x-y images at 340  $\mu\text{m}$  from the top surface: a.) LSCM and b.) HR-OCT.

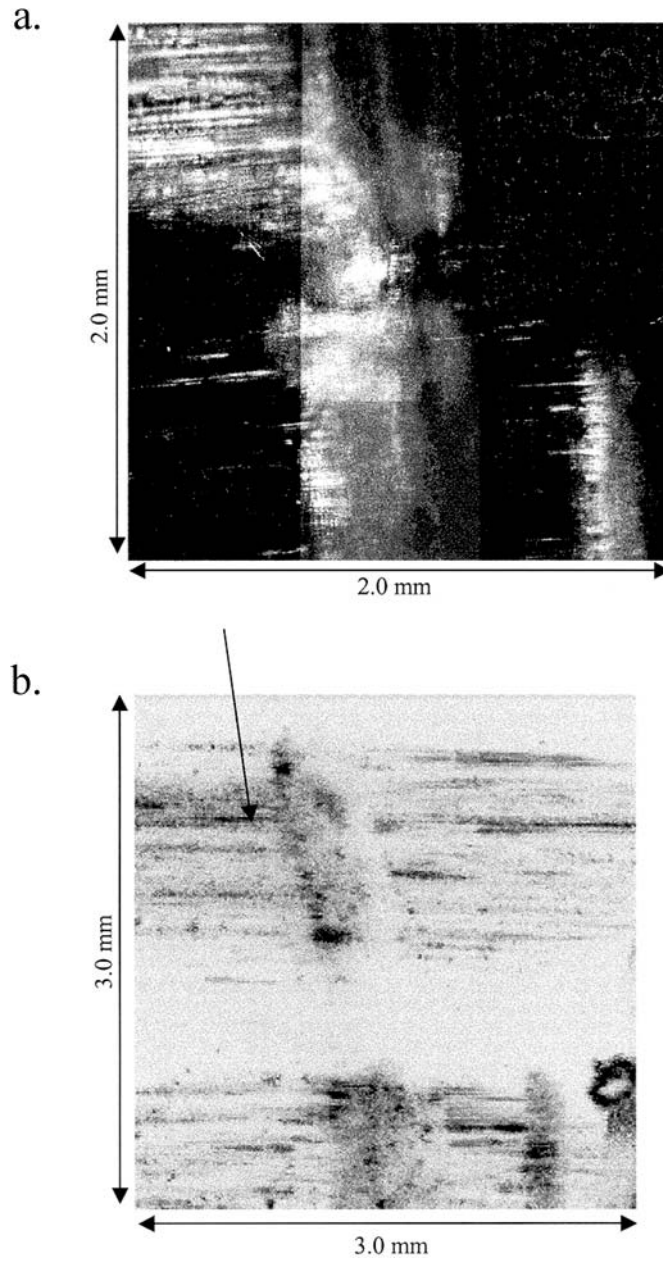


**FIGURE 9** Comparison of x-y images at 650 μm from the top surface: a.) LSCM and b.) HR-OCT.

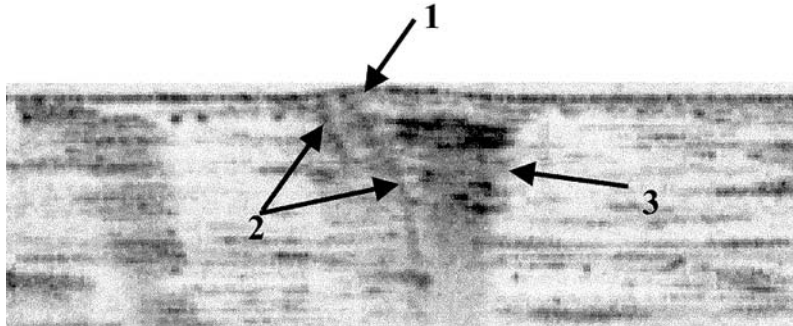


**FIGURE 10** HR-OCT of x-z plane showing displacement of the surface from kink bands, and fiber/matrix debonding.

Figure 12 compares the OCT and LSCM images 860  $\mu\text{m}$  from the surface. This distance probes the top of the second layer of fabric. The limitations of LSCM are very evident here. In Figure 12b, it is clear that the slice is in the second layer of fabric because the tows are displaced relative to the tows in the previous images. The tow itself is clearly differentiated from the damage. The corresponding LSCM image in Figure 12a exhibits poor contrast. What appears to be damage shown by arrow 1 is a stray light artifact from a bright feature above leaking into the image. The region indicated by arrow 2 may also be a stray light artifact or may be the actual reflection from the bottom of the first layer of fabric since that feature is also seen in the OCT. It is possible for the bottom portion of one layer of tows to reside in the same plane as the top portion of the underlying layer since layers with aligned tows may pack together with a nested architecture.

The difference in sensitivity between OCT and LSCM has to do with how these techniques reject stray light as manifested in the point-spread-function (PSF). In short, the PSF is the diffraction pattern of the image plane as brought to a focus by a lens [23]. It is the first dark fringe of this diffraction pattern, called the Airy disc, from which the majority of the light is transmitted and measured for resolution and sensitivity. PSFs are present for both the transverse and axial directions. For LSCM, the PSF in both the transverse and axial is narrowed, when compared by conventional microscopy, by detecting only the light that comes from the object that is conjugate to the detector and the source. This is accomplished by placing a variable pinhole at the detector and illuminating on the object plane with a coherent source (laser). Focal plane resolution is determined by the width of the

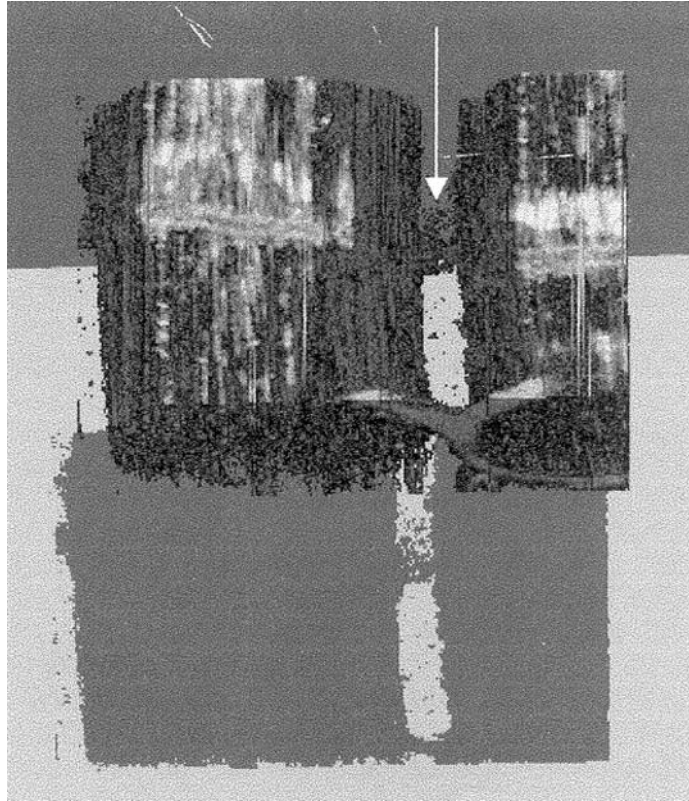


**FIGURE 11** Volumetric reconstruction of HR-OCT with certain grayscale values made invisible to show the region of diffuse matrix damage seen in LSCM.

Airy disk and the axial resolution is determined by its height. In the ideal confocal microscope, both are 1.3 times greater than for a conventional microscope [24]. The result of these improvements is that the confocal system has a slightly better resolution than a conventional microscope and a greatly improved rejection of stray light or sensitivity. In confocal microscopy, a point illumination falls off as the inverse square of distance from the focal plane. The improved sensitivity is manifested by the detection of light only to the first dark fringe of the diffraction pattern and not higher order fringes. Thus, objects within a plane and between image planes are better resolved. Details of the mathematics are given elsewhere [23]. With LSCM, the sensitivity is only as good as the ability of the pinhole to reject the stray light. Although the  $99\ \mu\text{m}$  pinhole used in this work was necessary to

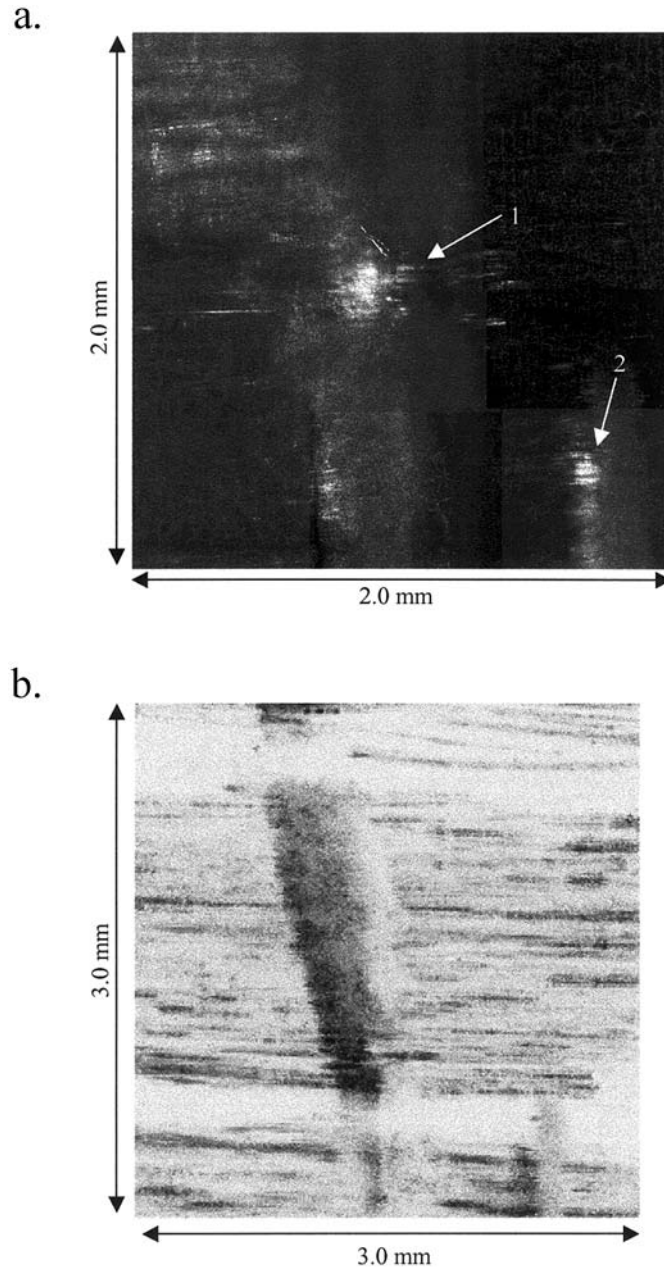


**FIGURE 12** Comparison of images at  $850\ \mu\text{m}$  from the top surface: a.) LSCM and b.) HR-OCT.

duplicate the OCT axial resolution of  $15\ \mu\text{m}$ , it may have not been sufficiently small to mask the higher order fringes of the PSF, resulting in the appearance of bright features from other planes.

The mechanism for stray light rejection for OCT is interferometric, not geometric. Therefore, the only noise contribution to the signal results from the shot-noise of the detector. According to Izatt et al. [25], for the same optical configuration, OCT has been shown to have substantially higher signal-to-noise and narrower point spread function than confocal microscopy. OCT does not have an advantage over LSCM for imaging features close to the surface, 5 scattering sites or less. For OCT, the ultimate resolution is solely determined by the bandwidth of the source in the axial direction and the numerical aperture of the focusing objective in the transverse direction. More discussion on the origin of the axial resolution is provided elsewhere [26]. Most recently, OCT and confocal have been combined by introducing a pinhole at the detector to improve OCT resolution and contrast [27].

## CONCLUSIONS

This work has compared the strengths and limitations of three non-destructive evaluation techniques for imaging a region of impact damage in an epoxy/E-glass composite. Optical coherence tomography is a highly sensitive technique that revealed the reinforcement architecture and damage with  $10\ \mu\text{m}$  to  $20\ \mu\text{m}$  spatial resolution. Information about the reinforcement architecture included the tow stacking arrangement and placement of the fabric stitching. A number of damage mechanisms were found and were identified as kink banding, fiber/matrix debonding, longitudinal cracking, and matrix deformation. All of these mechanisms were consistent with damage expected from bending a composite with a tough matrix and poor fiber-matrix bonding. The limitations of OCT were that the fiber architecture was not imaged clearly throughout the entire specimen thickness. The images were subject to artifacts such as shadowing, contrast degradation as a function of thickness, and degradation of spatial resolution. Image collection was automated and took on the average 3 to 5 h, depending on the size of the image set.

X-ray computed tomography clearly imaged the tow stacking throughout the entire sample but was not sensitive enough to detect the stitching. Because of sensitivity and resolution limitations, the fiber/matrix debonding and kink-band damage were seen together as one barely visible region. The matrix deformation was not visible. The 51 slices took 1.5 min per slice to collect or a total of 1.25 h.

The laser scanning confocal microscopy confirmed the high contrast features visible using the OCT, namely, the debonding and the matrix deformation. It is very difficult to confirm the presence of kink-bands using the LSCM images alone. The depth of usable images was far below that of OCT, about 700  $\mu\text{m}$  compared with 3 to 4 mm. Matching the thickness resolution of LSCM and OCT caused a stray light problem in the LSCM images. Also, the LSCM images were very time consuming to collect because the operator was required to adjust the brightness manually for every detection area.

## REFERENCES

- [1] Morita, H. and Tittman, B. R. *Rev. Prog. Quant. NDE* **16B**, 1885 (1997).
- [2] Downs, K. S. and Hamstead, M. A. *J. Comp. Mat.* **32**(3), 258 (1998).
- [3] Wooh, S.-C., Daniel, I. and Chun, H.-J. *Rev. Prog. Quant. NDE* **14B**, 1383 (1995).
- [4] Haque, A. and Raju, P. K. *Mat. Eval.* **56**(6), 765 (1998).
- [5] Ball, R. and Almond, D. *NDT & E Int.*, **31**(3), 165 (1998).
- [6] Highsmith, A. and Keshav, S. *J. Comp. Tech. & Res.* **19**(1), 10 (1997).
- [7] Kortschot, M. and Zhang, C. *Comp. Sci. & Tech.* **53**(2), 175 (1995).
- [8] Jones, T. and Berger, H. *Mat. Eval.* **47**, 390 (1989).
- [9] Huang, M., Jiang, L., Liaw, P., Brooks, C., Seeley, R. and Klarstrom, D. *JOM-e* **50**(11), 1998, <http://www.tms.org/pubs/journals/JOM/9811/Huang/Huang~9811.html>.
- [10] Krietsch, T. and Bohse, J. *Prog. in Acoustic Emission* **31**(1), S233 (1998).
- [11] Bates, D., Smith, G., Lu, D. and Hewett, J. *Composites, Part B* **31**(3), 175 (2000).
- [12] Sawatari, T. *Appl. Opt.* **12**(11), 2768 (1973).
- [13] Hee, M., Izatt, J., Swanson, E., Huang, D., Schuman, J., Lin, C., Puliafito, C. and Fujimoto, J. G. *Archives of Ophthalmology* **113**, 325 (1995).
- [14] Barton, J., Milner, T., Pfefer, T., Nelson, J. and Welch, A. *J. of Biomed. Opt.* **2**(2), 226 (1997).
- [15] Boppart, S., Brezinski, M., Bouma, B., Tearney, G. and Fujimoto, J. *Developmental Biology* **177**, 54 (1996).
- [16] Drexler, W., Morgner, U., Kartner, F. X., Pitris, C., Boppart, A., Li, X. D., Ippen, E. P. and Fujimoto, J. G. *Opt. Lett.* **24**(17), 1221 (1999).
- [17] Everett, M. J., Schoenengerger, K., Colston, Jr., B. W. and Da Silva, L. B. *Opt. Lett.* **23**(3), 228 (1998).
- [18] Bossi, R. and Georgeson, G. *Materials Evaluation* **53**(10), 1198 (1995).
- [19] Bach, P. H. Ed. *Biotechnology Applications of Microinjection, Microscopic Imaging, and Fluorescence* (Plenum Press, N. Y., 1993).
- [20] Dunkers, J. P., Parnas, R. S., Zimba, C. G., Peterson, R. S., Flynn, K. M., Fujimoto, J. G. and Bouma, B. E. *Composites, Part A* **30**, 139 (1999).
- [21] Identification of a commercial product is made only to facilitate experimental reproducibility and to adequately describe experimental procedure. In no case does it imply endorsement by NIST or imply that it is necessarily the best product for the experimental procedure.
- [22] Momose, A. *Nucl. Instr. and Meth. in Phys. Res. A* **352**, 622 (1995).
- [23] Webb, R. H. *Rep. Prog. Phys.* **59**, 427 (1996).
- [24] Sandison, D. H. and Webb, W. W. *Appl. Opt.* **33**(4), 603 (1994).
- [25] Izatt, J. A., Hee, M. R., Owen, G. M., Swanson, E. A. and Fujimoto, J. G. *Opt. Lett.* **19**(8), 590 (1994).

- [26] Swanson, E. A., Huang, D., Hee, M. R., Fujimoto, J. G., Lin, C. P. and Puliafito, C. A. *Opt. Lett.* **17**(2), 151 (1992).
- [27] Xu, F., Pudavar, H. E., Prasad, P. N. and Dickensheets, D. *Opt. Lett.* **24**(24), 1808 (1999).